Neurobiology of Aging 73 (2019) 92–103

Contents lists available at ScienceDirect

Neurobiology of Aging

journal homepage: www.elsevier.com/locate/neuaging

Dendritic spine remodeling accompanies Alzheimer's disease pathology and genetic susceptibility in cognitively normal aging

Benjamin D. Boros [a,b], Kelsey M. Greathouse [a,b], Marla Gearing [c], Jeremy H. Herskowitz [a,b,*]

[a] Center for Neurodegeneration and Experimental Therapeutics, University of Alabama at Birmingham, Birmingham, AL, USA
[b] Department of Neurology, University of Alabama at Birmingham, Birmingham, AL, USA
[c] Department of Pathology, Department of Neurology, Laboratory Medicine, Emory University School of Medicine, Atlanta, Georgia

ARTICLE INFO

Article history:
Received 1 May 2018
Received in revised form 5 September 2018
Accepted 6 September 2018
Available online 21 September 2018

Keywords:
Alzheimer's disease
Aging
Dendritic spine
APOE
Prefrontal cortex
Dementia
Resiliency

ABSTRACT

Subtle alterations in dendritic spine morphology can induce marked effects on connectivity patterns of neuronal circuits and subsequent cognitive behavior. Past studies of rodent and nonhuman primate aging revealed reductions in spine density with concomitant alterations in spine morphology among pyramidal neurons in the prefrontal cortex. In this report, we visualized and digitally reconstructed the three-dimensional morphology of dendritic spines from the dorsolateral prefrontal cortex in cognitively normal individuals aged 40–94 years. Linear models defined relationships between spines and age, Mini–Mental State Examination, apolipoprotein E (APOE) ε4 allele status, and Alzheimer's disease (AD) pathology. Similar to findings in other mammals, spine density correlated negatively with human aging. Reduced spine head diameter associated with higher Mini–Mental State Examination scores. Individuals harboring an APOE ε4 allele displayed greater numbers of dendritic filopodia and structural alterations in thin spines. The presence of AD pathology correlated with increased spine length, reduced thin spine head diameter, and increased filopodia density. Our study reveals how spine morphology in the prefrontal cortex changes in human aging and highlights key structural alterations in selective spine populations that may promote cognitively normal function despite harboring the APOE ε4 allele or AD pathology.

1. Introduction

Information processing and higher-order cognitive tasks rely on the capability to remodel, gain, or lose synaptic connections. In contrast to widespread circuit collapse in Alzheimer's disease (AD) dementia, age-related cognitive impairment likely involves slight alterations in networks responsible for executive control and/or learning and memory (Burke and Barnes, 2006; Dickstein et al., 2012). Diverse lines of evidence in aged rodents (Barnes et al., 1997; Petralia et al., 2014; Smith et al., 2000) and nonhuman primates (Bai et al., 2004; Luebke et al., 2004; Peters et al., 1996, 2008) suggest that these network connections exhibit deficits in mechanisms underlying synaptic transmission in the absence of robust neuronal structure deterioration. Examining the relationships between age and commonly occurring AD neuropathology with synaptic remodeling or loss may inform on strategies to limit cognitive decline in humans.

Most excitatory synapses occur on actin-rich protrusions along neuronal dendrites called dendritic spines, and synapse strength and activity are inseparably linked to the structural plasticity or remodeling of spine morphology (Hayashi and Majewska, 2005). Over the course of mammalian life synaptic activity influences the number and shape of spines, notably, in brain development, behavioral learning, and aging (Alvarez and Sabatini, 2007; Holtmaat and Svoboda, 2009; Kasai et al., 2010). Live imaging studies indicate that spines can change size and shape over time-scales of seconds to minutes and hours to days (Parnass et al., 2000). Spine structure is inextricably linked to spine function, and spines can be generally classified on the basis of their three-dimensional morphology as stubby, mushroom, or thin (Chang and Greenough, 1984; Harris et al., 1992; Hering and Sheng, 2001; Peters and Kaiserman-Abramof, 1970). Stubby spines are hypothesized to be transitional structures that will enlarge, possibly to mushroom spines, which represent more stable structures with a wide head and thin neck. Thin spines are more dynamic and lack the wide, stable head indicative of mature mushroom-shaped spines. The volume of the spine head is directly proportional to the density of receptors at the postsynaptic tip and regulates

* Corresponding author at: Departments of Neurology and Neurobiology, Center for Neurodegeneration and Experimental Therapeutics, University of Alabama at Birmingham, 1825 University Boulevard, Birmingham, AL 35294, USA. Tel.: +205 996 6257; fax: +205 996 1556.
E-mail address: jhersko@uab.edu (J.H. Herskowitz).

0197-4580/$ – see front matter © 2018 Elsevier Inc. All rights reserved.
https://doi.org/10.1016/j.neurobiolaging.2018.09.003

calcium equilibrium by promoting efficient diffusion of calcium through the neck of the spine (Majewska et al., 2000a,b; Nusser et al., 1998; Yuste et al., 2000). Spine neck structural plasticity regulates excitatory postsynaptic potential while controlling the biochemical compartmentalization of the overall spine shape (Tonnesen et al., 2014). Finally, dendritic filopodia are actin-rich protrusions that are widely considered the precursors of dendritic spines (Ziv and Smith, 1996).

The dorsolateral prefrontal cortex (DLPFC) Brodmann area 46 (BA46) is tightly linked to cognitive performance, including working memory, and is highly vulnerable in age-related memory loss and neurodegenerative disorders in primates and humans, respectively (Dumitriu et al., 2010; van Veluw et al., 2012; Wong et al., 2014). Nonhuman primate studies of area 46 report significant changes in spine density and morphology with aging, including spine loss and reduction of excitatory synapses (Cupp and Uemura, 1980; Dickstein et al., 2012; Duan et al., 2003; Dumitriu et al., 2010; Page et al., 2002; Peters et al., 1998). More specifically, selective loss of thin spines correlated strongly with impaired ability of aged rhesus monkeys to learn a delayed nonmatching-to-sample task (Dumitriu et al., 2010). These findings suggest that reduction of this spine type may negatively affect prefrontal synaptic plasticity that is crucial for normal cognition in aging (Morrison and Baxter, 2012).

Cognitive decline in AD is the result of synapse loss in brain regions that are critical for memory processes. This is based on numerous reports demonstrating that synaptic markers and/or dendritic spine loss correlate more strongly with cognitive impairment in AD than amyloid-β (Aβ) plaques or neurofibrillary tangles (NFTs) (Boros et al., 2017; DeKosky and Scheff, 1990; Terry et al., 1991). Recently, we developed methods that allow three-dimensional modeling of dendritic spines from brightfield microscopy images of postmortem human brain tissue samples. These studies revealed that maintenance of thin and mushroom spine populations combined with cumulative increased spine extent in the DLPFC distinguished cognitively normal older individuals with AD pathology from patients with AD dementia (Boros et al., 2017). These observations provided cellular evidence to support the hypothesis that remodeling of dendritic spine structure may be a mechanism of cognitive resilience that protects older individuals with AD pathology from developing dementia. Using our image analysis strategies, we present novel findings in this report, which highlight morphologic attributes of prefrontal dendritic spines that associate with positive cognitive performance, the apolipoprotein E (APOE) gene ε4 allele, and AD pathology in human aging.

2. Methods

2.1. Human brain tissue

Samples of BA46 DLPFC were collected at the Emory University Alzheimer's Disease Research Center (ADRC) (Table 1). Some cases exhibited a range of AD pathology, but all were cognitively normal at death. Cognitive status was determined by Mini–Mental State Examination (MMSE). The MMSE is the most commonly used test for complaints of memory impairment or when a diagnosis of dementia is being considered. Notably, patients with severe to moderate AD have MMSE scores of 10–20 of total possible of 30 (Hughes et al., 1982; Morris, 1993). AD-related pathology was measured based on Consortium to Establish a Registry for Alzheimer's Disease (CERAD) criteria for the neuropathological diagnosis of AD and Braak staging of neurofibrillary pathology. The majority of these cases had no coexisting pathologies, such as stroke or Lewy body pathology. Neuritic and diffuse plaques were scored semi-quantitatively according to CERAD methods (Mirra et al., 1991). CERAD (0→3, or none, sparse, moderate, or frequent) and Braak (0→6) scores are measures for the severity of neuritic plaque and NFT accumulation, respectively. The Amyloid Braak CERAD score was used as a global measure of AD pathology (Montine et al., 2012). Cases were matched as closely as possible for sex and postmortem interval (PMI). Previous studies and regression analyses from our group demonstrated that sex or PMI does not correlate with spine phenotypes (Boros et al., 2017).

2.2. Tissue processing and Golgi-Cox staining

All tissue samples were processed and stained as previously described (Boros et al., 2017). Briefly, tissue samples were fixed in

Table 1
Clinical and neuropathologic data on postmortem human brain tissue samples

Case	Race/sex	Age (y)	APOE	MMSE	Braak stage	CERAD score	ABC score	PMI (hours)
1	WF	40	ε3/4		0	0	None	31
2	BM	46	ε3/3		0	0	None	6.5
3	WF	52	ε3/4		0	B	Low	3
4	WM	56			I	0	None	12.5
5	BM	59	ε2/3		I	0	None	6
6	BF	61			II	0	None	6
7	BM	61	ε3/4		II	0	Low	12
8	WF	64	ε4/4	30	II	C	low	17
9	BM	70	ε3/3	29	I	0	None	2.5
10	WF	75	ε3/3	29	I	0	None	6
11	WM	76	ε2/4	29	IV	C	Intermediate	35.5
12	WF	78	ε3/3	30	II	0	None	11.5
13	WM	80	ε3/4	28	IV	C	Intermediate	5.5
14	WM	81	ε3/3	27	II	B	low	20
15	WF	82	ε3/4	30	III	C	Intermediate	38
16	WM	87	ε3/4	27	I	B	Intermediate	20.5
17	WF	87	ε2/3		III	C	Intermediate	5
18	WF	88	ε2/4	26	II	0	None	14.5
19	WM	89	ε3/3	27	IV	C	Intermediate	19
20	WF	91	ε3/3	29	III	A	Low	6
21	WF	92	ε3/3	30	III	0	None	15.5
22	WM	94	ε3/3	29	II	0	None	5.5

If values are blank, information was not available.
Key: ABC, Amyloid Braak CERAD; APOE, apolipoprotein E; B, black/African American; CERAD, Consortium to Establish a Registry for Alzheimer's Disease; F, female; M, male; MMSE, Mini–Mental State Examination; PMI, postmortem interval; W, white/Caucasian.

4% paraformaldehyde following dissection and stored in sodium azide preservative solution at 4 °C. Tissue blocks of ~20 × 20 × 35 mm were sectioned into 250-μm slices with a Leica vibratome (VT1000s; Leica Biosystems, Buffalo Grove, IL, USA) and stored in preservation buffer (0.1% wt/vol sodium azide in phosphate-buffered saline) until Golgi-Cox impregnation. Tissues were stained using the FD Rapid Golgi Stain Kit (PK401, FD Neurotechnologies, Columbia, MD, USA) and manufacturer's instructions. Tissues were impregnated in a chromate solution (potassium dichromate, mercuric chloride, and potassium chromate) for 6 weeks. Next, tissues were immersed in Solution C for 48 hours with replacement after 24 hours. Tissues were plated on 75 × 25 mm gelatin-coated slides (PO101; FD Neurotechnologies) and allowed to dry. Slides were submerged sequentially in mixtures of Solution D, Solution E, and distilled water. Next, tissues were dehydrated with graded alcohols (70%, 90%, and 100% ethanol in deionized water) and cleared with xylenes (X3P-1GAL; Thermo Fisher Scientific, Waltham, MA, USA). Slides were sealed with Permount Toluene Solution (SP15-100; Fisher Chemicals, Fair Lawn, NJ, USA) and cover-slipped with spacers (Secure Seal Spacer, 20 mm diameter × 0.12 mm depth, 70,327-205; Electron Microscopy Sciences, Hatfield, PA, USA) and 50 × 24 mm glass (cover glass, rectangles, 24 × 50 mm, thickness 0.13–0.17 mm, 633,153; Carolina Biological, Burlington, NC, USA).

2.3. Dendrite imaging

Images of neuronal basal dendrites from BA46 DLPFC layers II and III were captured as previously described (Boros et al., 2017). For each case, many tissue slices were Golgi-stained. From each tissue slice, two or more cells were imaged and analyzed; 10-20 Golgi-stained cells were sampled per case. From each cell, a single basal dendritic segment was imaged. The following criteria were used to select cells for imaging: (1) located centrally within the tissue sample depth; (2) not obscured by large staining debris; and (3) fully impregnated. If the cell met the criteria, a single dendritic length was imaged. Dendrite selection criteria were (1) unobstructed/isolated/not overlapping other dendrites; (2) dendrite length greater than 30 μm; and (3) dendrite diameter approximately 1 μm. If more than two basal dendrites fulfilled the criteria from a single cell, the first dendrite clockwise was the only dendrite selected. If no dendrites from a cell fulfilled the criteria, another cell was viewed and scrutinized. All imaging was conducted by a single, blinded experimenter. Each tissue slice was initially viewed under low 4x magnification to establish the region of interest (layers II and III). Next, a pyramidal cell basal dendrite within the region of interest was viewed at 60× magnification to determine if the basal dendrite fulfilled the aforementioned criteria. A maximum of two dendrites were imaged per tissue slice. Z-stacks were captured with a z-step size of 0.1 μm. Each image was recorded using the following parameters: lamp: 100; field stop: 1.5 mm; exposure: 60 ms; analog gain: 2.0× - 2.4×; and image size: 1028 × 1028 (0.1619 μm × 0.1619 μm × 0.1 μm). Images were captured on a Nikon Eclipse Ni upright microscope (Tokyo, Japan) with Lumen 200 light source (Prior Scientific, Rockland, MA, USA) and Nikon DS-43 Digital Sight for brightfield microscopy and Nikon Elements 4.20.02. A 60× oil immersion objective (Nikon Plan Apo, N.A. 1.40) was used.

2.4. Three-dimensional digital image reconstruction

Dendrite and spine reconstructions were conducted by a single, blinded experimenter as previously described (Boros et al., 2017). Briefly, image stacks were imported to Neurolucida 360 (2.70.1; MBF Biosciences, Williston, Vermont). Dendrites were traced using a semiautomated directional kernel algorithm. Spines were traced using voxel clustering. When possible, we followed the basal dendrite from soma to tip. Initiation and termination points for dendrite reconstruction were established using the following criteria: must be ≥10 μm away from the distal tip of the dendrite; must contain consistent dendrite diameter; must have a level axis with limited movement in the z plane; and must be ≥30 μm in length. The experimenter manually scrutinized each assigned point in the x, y, and z plane to verify the point was located on the dendrite or spine and not incorrectly assigned. Points were scrutinized first by viewing the dendrite at individual x-z or y-z planes and by ensuring that points were correctly positioned at midline of the dendrite. Then, points were verified in the x-y plane, and the diameter of each point was confirmed to match the dendrite diameter. Dendritic spine reconstruction used the following parameters for classification—outer range: 7.0 μm; minimum height: 0.3 μm; detector sensitivity: 90-125; and minimum count: 8 voxels. Dendritic spines were traced as the experimenter traversed the full dendrite z plane and inspected the x-y plane at each individual z-step. The morphology of each reconstructed spine was carefully scrutinized, and if necessary, the merge and slice tools were used to correct inconsistencies of spine assignment by Neurolucida 360. Spine backbone was used in recording spine length and spine classification. The positioning of each backbone point (including point of greatest breadth) was confirmed by the experimenter. To correct a misrepresentative backbone, the spine was viewed from the z plane, and experimenter moved backbone points in the x-y plane. Any repositioning in the x-z or y-z plane was performed while the spine was being viewed from the lateral angle.

Morphometric analysis was performed for each spine, and measurements categorized spines into thin, stubby, mushroom, or filopodia classes. Spine classification followed established parameters, as previously described (Boros et al., 2017; Swanger et al., 2011, 2015). For spine classification, the following established parameters were used—head-to-neck ratio: 1.1; length-to-head ratio: 2.5; mushroom head size: 0.35 μm; and filopodium length: 3.0 μm. Spines with a head-to-neck ratio greater than 1.1 and head diameter greater than 0.35 μm were classified as mushroom. Spines were classified as filopodia or thin, if head-to-neck ratio was less than 1.1, and either (1) length-to-head ratio was greater than 2.5 or (2) head size was less than 0.35 μm. Of these, if the total length was greater than 3.0 μm, the spine was classified as filopodia; if less than 3.0 μm, thin. Spine density was defined as the number of spines per 10 μm of dendrite length. Spine length was defined as the curvilinear length from the base of the dendrite shaft to the most distal point of the spine head. Head diameter was defined as the breadth of the spine head at its widest cross-sectional point.

Previous investigations using electron microscopy in aged humans exhibit strong similarities to our reported spine length and head diameter measurements (Jacobs et al., 1997, 2001; Rask-Andersen et al., 2000). Additional studies measuring spine structure characteristics in human and nonhuman primates using confocal and light microscopy report spine measurements that are highly consistent with our findings (Benavides-Piccione et al., 2002, 2013; Tang et al., 2014; Young et al., 2014).

2.5. Statistical analysis

Statistical analysis was performed using SPSS Statistics, version 25, (IBM Corporation, Armonk, NY, USA) and Prism 6.0 (GraphPad Software, La Jolla, CA, USA). Data are presented as mean ± standard error of the mean (SEM), and all graph error bars represent SEM. All statistical tests had threshold of statistical significance set at $p < 0.05$. Case mean values for spine head diameter, length, or number of spines per 10 μm was generated by averaging 10-20 dendrite mean values across each case. A dendrite mean for each

Table 2
Linear correlations between age and dendritic spine phenotypes

Dependent variable	Pearson regression		Unadjusted	
	r	*p*	β	*p*
Spine density (per 10 μm)	−0.473	0.013	−0.064	0.026
Spine length (μm)	0.082	0.358	0.001	0.716
Head diameter (μm)	0.009	0.485	0.000	0.969
Thin spine density (per 10 μm)	−0.326	0.070	−0.034	0.139
Stubby spine density (per 10 μm)	−0.349	0.056	−0.029	0.112
Mushroom spine density (per 10 μm)	−0.049	0.415	−0.002	0.829
Filopodia density (per 100 μm)	−0.064	0.388	−0.001	0.776
Thin spine length (μm)	0.218	0.164	0.003	0.329
Stubby spine length (μm)	0.188	0.201	0.002	0.402
Mushroom spine length (μm)	−0.046	0.419	−0.001	0.837
Filopodia length (μm)	0.202	0.301	−0.002	0.691
Thin spine head diameter (μm)	0.000	0.500	0.000	0.999
Stubby spine head diameter (μm)	−0.027	0.453	0.000	0.906
Mushroom spine head diameter (μm)	0.264	0.118	0.002	0.236
Filopodia head diameter (μm)	−0.077	0.422	−0.005	0.447

Pearson regressions were performed for each comparison, and Pearson's coefficient (r) is reported.
These relationships were further examined in a multivariate model between age (independent variable) and each spine variable (dependent variable).
For these comparisons, the unstandardized β coefficient (β) is reported.

morphological parameter was generated by averaging the length or head diameter of all spines on a single dendrite. Statistical comparisons included simple linear regression, multivariate linear regression, and two-tailed unpaired t-tests. Unadjusted or adjusted linear modeling characterized the relationship between clinicopathologic factors with each spine phenotype. Factors of interest included age, APOE ε4 status, Braak stage, CERAD scores, and MMSE scores. Pearson's linear regression was performed and reported for each comparison. Unadjusted linear models assessed associations involving age, APOE ε4 status, Braak stage, CERAD scores, and MMSE scores. Adjusted models were also used to characterize relationships involving MMSE (age-adjusted), Braak stage (APOE-adjusted), CERAD scores (APOE-adjusted), and APOE status (Braak stage–adjusted and CERAD-adjusted). Each spine phenotype was entered as a dependent variable in models involving age, APOE status, Braak stage, and CERAD scores. MMSE was entered as the dependent variable in comparisons with spine phenotype predictors. The relationship between APOE ε4 and spine phenotypes was further characterized by a two-tailed *t*-test comparing ε4 carriers (n = 11) with non-ε4 carriers (n = 9). For linear models, APOE ε4 status was coded with carriers = 1 and noncarriers = 0. All regression graphs depict a simple linear regression and corresponding Pearson coefficient. Tables 2–5 list each comparison and corresponding unstandardized β coefficient, Pearson's coefficient, *t* value, or *p* value.

3. Results

3.1. Prefrontal dendritic spine density is reduced in human aging

In a cohort aged 40–94 years (mean: 73.1) (Table 1), we quantitatively measured the density and structure of dendritic spine populations from BA46 DLPFC layer II and III basal dendrites. We visualized dendritic structure using an optimized Golgi-Cox impregnation strategy coupled with brightfield microscopy and three-dimensional digital reconstruction of dendrites and spines (Fig. 1). To test whether spine density or morphology is altered in aging, we measured the relationship between age and spine density or morphology using Pearson's regression and a multivariate linear regression model (with age as a predictor). Spine density was

Table 3
Linear correlations between MMSE scores and dendritic spine phenotypes

Independent variable	Pearson regression		Unadjusted	
	r	*p*	β	*p*
Spine density (per 10 μm)	0.345	0.113	0.216	0.226
Spine length (μm)	0.212	0.233	1.099	0.466
Head diameter (μm)	−0.477	0.042	−6.899	0.085
Thin spine density (per 10 μm)	0.407	0.074	0.332	0.149
Stubby spine density (per 10 μm)	−0.016	0.479	−0.016	0.958
Mushroom spine density (per 10 μm)	0.052	0.431	0.081	0.861
Filopodia density (per 100 μm)	0.256	0.189	1.799	0.378
Thin spine length (μm)	0.401	0.078	2.825	0.155
Stubby spine length (μm)	−0.295	0.153	−2.372	0.306
Mushroom spine length (μm)	0.381	0.089	1.971	0.178
Filopodia length (μm)	0.040	0.459	0.206	0.918
Thin spine head diameter (μm)	−0.001	0.499	−0.039	0.997
Stubby spine head diameter (μm)	−0.299	0.149	−2.561	0.299
Mushroom spine head diameter (μm)	−0.305	0.144	−3.136	0.289
Filopodia head diameter (μm)	−0.018	0.481	−0.140	0.962

Pearson regressions were performed for each comparison, and Pearson's coefficient (r) is reported.
These relationships were examined in a multivariate model between MMSE (dependent variable) and each spine variable (independent variable). Given the considerable influence of age on spines, these relationships were also examined in an age-adjusted linear model.
For these comparisons, the unstandardized β coefficient (β) is reported.
Key: MMSE, Mini–Mental State Examination.

Table 4
Comparisons between APOE ε4 status and dendritic spine phenotypes

Dependent variable	Mean ± SEM		*t*-test	
	Non-ε4	ε4	*t*	*p*
Spine density (per 10 μm)	9.332 ± 0.627	9.547 ± 0.807	−0.214	0.833
Spine length (μm)	1.219 ± 0.064	1.36 ± 0.094	−1.272	0.220
Head diameter (μm)	0.573 ± 0.022	0.562 ± 0.036	0.288	0.777
Thin spine density (per 10 μm)	3.505 ± 0.401	4.359 ± 0.584	−1.241	0.231
Stubby spine density (per 10 μm)	3.443 ± 0.347	2.845 ± 0.524	0.982	0.339
Mushroom spine density (per 10 μm)	2.085 ± 0.252	2.063 ± 0.255	0.060	0.952
Filopodia density (per 100 μm)	0.07 ± 0.027	0.281 ± 0.07	−3.006	0.008
Thin spine length (μm)	1.309 ± 0.058	1.333 ± 0.071	−0.261	0.797
Stubby spine length (μm)	0.848 ± 0.049	0.847 ± 0.047	0.010	0.992
Mushroom spine length (μm)	1.517 ± 0.079	1.746 ± 0.1	−1.812	0.087
Filopodia length (μm)	3.522 ± 0.057	3.742 ± 0.106	−1.620	0.136
Thin spine head diameter (μm)	0.253 ± 0.006	0.214 ± 0.008	3.930	0.001
Stubby spine head diameter (μm)	0.755 ± 0.036	0.868 ± 0.062	−1.663	0.114
Mushroom spine head diameter (μm)	0.747 ± 0.033	0.748 ± 0.042	−0.016	0.987
Filopodia head diameter (μm)	0.447 ± 0.096	0.22 ± 0.025	2.661	0.024

Dependent variable	Pearson regression		Unadjusted		CERAD-adjusted		Braak stage–adjusted	
	Non-ε4	ε4	*t*	*p*	β	*p*	β	*p*
Spine density (per 10 μm)	0.050	0.416	0.216	0.833	−0.009	0.994	0.216	0.832
Spine length (μm)	0.287	0.110	0.141	0.220	0.075	0.519	0.141	0.152
Head diameter (μm)	−0.068	0.388	−0.012	0.777	−0.012	0.792	−0.012	0.783
Thin spine density (per 10 μm)	0.281	0.115	0.854	0.231	0.625	0.411	0.854	0.243
Stubby spine density (per 10 μm)	−0.226	0.170	−0.598	0.339	−0.259	0.686	−0.598	0.261
Mushroom spine density (per 10 μm)	−0.014	0.476	−0.022	0.952	−0.221	0.564	−0.022	0.952
Filopodia density (per 100 μm)	0.578	0.004	0.210	0.008	0.186	0.024	0.210	0.003
Thin spine length (μm)	0.061	0.399	0.024	0.797	−0.001	0.989	0.024	0.782
Stubby spine length (μm)	−0.002	0.496	−0.001	0.992	−0.041	0.564	−0.001	0.991
Mushroom spine length (μm)	0.393	0.043	0.229	0.087	0.213	0.142	0.229	0.071
Filopodia length (μm)	0.456	0.068	0.220	0.136	0.230	0.170	0.229	0.147
Thin spine head diameter (μm)	−0.680	0.000	−0.038	0.001	−0.030	0.005	−0.038	0.0003
Stubby spine head diameter (μm)	0.365	0.057	0.114	0.114	0.083	0.267	0.114	0.113
Mushroom spine head diameter (μm)	0.004	0.494	0.001	0.987	−0.001	0.990	0.001	0.987
Filopodia head diameter (μm)	−0.644	0.012	−0.226	0.024	−0.200	0.061	−0.204	0.031

The mean spine head diameter, length, or density of spines per 10 μm was compared between non-ε4 carriers (n = 9) and ε4 carriers (n = 11) by two-tailed Student's *t*-test. The mean ± standard error of the mean and *t* values were reported. Pearson regressions were performed by dummy-coding non-ε4 carrier = 0 and ε4 carrier = 1, and Pearson's coefficient (r) is reported. These relationships were further examined in a multivariate model between APOE ε4 status (independent variable) and each spine variable (dependent variable). Given the association between pathology and APOE status, these relationships were also examined in CERAD-adjusted and Braak stage–adjusted models. For these comparisons, the unstandardized β coefficient (β) is reported.

negatively correlated with advanced age in both simple regression ($r = -0.473$, $p = 0.013$) and our linear model ($\beta = -0.064$, $p = 0.026$) (Fig. 2A, Table 2). Next, we examined whether age associated with density of filopodia or thin, stubby, or mushroom spines. Although not statistically significant, age and density of thin ($r = -0.326$, $p = 0.070$) or stubby ($r = -0.349$, $p = 0.056$) spines were trending by simple regression (Fig. 2D, Table 2). Notably, spine density did not correlate with PMI ($r = -0.084$, $p = 0.363$) (Fig. 2C). Filopodia can sprout in responsive to hypoxic injury in cultured neurons (Park et al., 1996), so we measured the relationship between PMI and filopodia density using Pearson's regression and a multivariate linear regression model (with PMI as a predictor). Filopodia density positively correlated with PMI in simple regression ($r = 0.415$, $p = 0.034$) but not our linear model ($\beta = 0.001$, $p = 0.068$). Age did not associate with spine length or head diameter (Fig. 2E–F). Similar to rodents and nonhuman primates, spine density is reduced in the DLPFC with age among humans (Dickstein et al., 2012).

3.2. Higher MMSE scores correlate with reduced dendritic spine head diameter

Next, we tested whether MMSE scores associate with density or morphology of DLPFC spines using simple linear regression. Then, we further probed these potential relationships in an age-controlled univariate model (with spine phenotypes as predictors) to discriminate impairment from age-related spine changes (Table 3). MMSE scores did not correlate with overall spine density, spine classification densities, or mean spine length (Fig. 3A–C). Mean spine head diameter was negatively associated with MMSE scores in a statistically significant manner by simple regression ($r = -0.477$, $p = 0.042$) but did not reach significance in an age-adjusted model ($p = 0.085$) (Fig. 3D, Table 3). These findings emphasize spine head diameter in the DLPFC as a potential critical substrate for maintaining cognitive function in human aging. Association of thin spine density and MMSE scores by simple regression was trending but not significant ($r = 0.407$, $p = 0.074$) (Table 3). Correlation of thin spine length with MMSE scores was trending but did not reach significance by simple regression ($r = 0.401$, $p = 0.078$) or in an age-adjusted model ($\beta = 2.825$, $p = 0.155$) (Table 3). Notably, past studies in aged rhesus monkeys identified analogous associations between area 46 thin spines and cognitive function (Dumitriu et al., 2010).

3.3. APOE ε4 allele correlates with increased filopodia density and reduced thin spine head diameter

The human APOE gene exists as three polymorphic alleles: ε2, ε3, and ε4. The APOE ε4 allele is the strongest risk factor for late-onset AD, and the risk for AD is 2- to 3-fold higher in patients with one APOE ε4 allele and approximately 12-fold higher with two APOE ε4 alleles (Corder et al., 1993; Farrer et al., 1997; Michaelson, 2014; Saunders et al., 1993). About 60% of Caucasian AD patients are

Table 5
Linear correlations between CERAD or Braak stage and dendritic spine phenotypes

Dependent variable	Independent variable	Pearson regression		Unadjusted		APOE-adjusted	
		r	*p*	β	*p*	β	*p*
Spine density (per 10 μm)	*Braak Stage*	−0.292	0.094	−0.501	0.188	−0.435	0.284
	CERAD	0.085	0.353	0.136	0.706	0.234	0.574
Spine length (μm)	*Braak Stage*	0.542	0.005	0.105	0.009	0.105	0.012
	CERAD	0.456	0.017	0.081	0.033	0.069	0.120
Head diameter (μm)	*Braak Stage*	0.003	0.494	0.000	0.989	−0.002	0.884
	CERAD	−0.071	0.377	−0.005	0.754	0.000	0.984
Thin spine density (per 10 μm)	*Braak Stage*	−0.135	0.275	−0.179	0.549	−0.099	0.725
	CERAD	0.229	0.153	0.280	0.306	0.239	0.399
Stubby spine density (per 10 μm)	*Braak Stage*	−0.527	0.006	−0.560	0.012	−0.581	0.011
	CERAD	−0.411	0.029	−0.403	0.058	−0.353	0.151
Mushroom spine density (per 10 μm)	*Braak Stage*	0.212	0.172	0.127	0.344	0.141	0.337
	CERAD	0.262	0.119	0.146	0.238	0.207	0.156
Filopodia density (per 100 μm)	*Braak Stage*	0.469	0.014	0.068	0.028	0.065	0.013
	CERAD	0.399	0.033	0.053	0.066	0.025	0.386
Thin spine length (μm)	*Braak Stage*	0.426	0.024	0.066	0.048	0.065	0.065
	CERAD	0.239	0.143	0.034	0.285	0.026	0.486
Stubby spine length (μm)	*Braak Stage*	0.496	0.009	0.056	0.019	0.059	0.025
	CERAD	0.327	0.069	0.034	0.137	0.042	0.124
Mushroom spine length (μm)	*Braak Stage*	0.367	0.047	0.085	0.093	0.086	0.084
	CERAD	0.240	0.141	0.051	0.282	0.016	0.759
Filopodia length (μm)	*Braak Stage*	0.129	0.370	−0.009	0.888	−0.020	0.733
	CERAD	0.183	0.319	0.004	0.932	−0.008	0.874
Thin spine head diameter (μm)	*Braak Stage*	−0.384	0.039	−0.009	0.077	−0.008	0.025
	CERAD	−0.519	0.007	−0.011	0.013	−0.008	0.031
Stubby spine head diameter (μm)	*Braak Stage*	0.259	0.122	0.033	0.245	0.029	0.286
	CERAD	0.337	0.063	0.039	0.126	0.032	0.252
Mushroom spine head diameter (μm)	*Braak Stage*	0.224	0.159	0.020	0.317	0.020	0.342
	CERAD	−0.018	0.468	−0.001	0.937	0.002	0.939
Filopodia head diameter (μm)	*Braak Stage*	−0.579	0.051	−0.077	0.306	−0.052	0.140
	CERAD	−0.482	0.095	−0.084	0.160	−0.024	0.469

Pearson regressions were performed for each comparison, and Pearson's coefficient (r) is reported. These relationships were further examined in a multivariate model between either CERAD or Braak stage (dependent variable) and each spine variable (independent variable). Given the considerable influence of APOE ε4 status, these relationships were also examined in an APOE ε4–adjusted linear model. For these comparisons, the unstandardized β coefficient (β) is reported.

APOE ε4 carriers, and this can reduce the age of AD onset in a gene dose-dependent manner nearly 7–9 years per allele copy (Corder et al., 1993). Therefore, we tested whether cognitively normal individuals with at least a single ε4 allele (n = 9) exhibit differences in spine density or morphology compared with non-ε4 carriers (n = 11). Notably, there was no difference between groups in mean age (t = 1.174, $p = 0.256$) or MMSE scores (t = 0.559, $p = 0.608$). Increased filopodia density was observed among ε4 carriers compared with non-ε4 carriers (t = −3.01, $p = 0.008$) (Fig. 4C, Table 4), but no differences in density of thin, stubby, or mushroom spines were detected (Fig. 4A–B). Next, we examined how ε4 status associates with spine morphology. This revealed that ε4 carriers exhibited significantly reduced thin spine head diameter (t = 3.93, $p = 0.001$) (Fig. 4F, Table 4). Next, we examined these relationships in a CERAD or Braak stage–adjusted model with APOE status as a predictor of each spine phenotype. In the CERAD-adjusted model, the APOE ε4 allele maintained a significant association with increased filopodia density (β = 0.186, $p = 0.024$) and reduced thin spine head diameter (β = −0.030, $p = 0.005$). APOE ε4 trended with increased mushroom spine length (β = 0.213, $p = 0.142$) after controlling for CERAD scores (Table 4). In the Braak stage–adjusted model, the ε4 allele was correlated significantly with increased filopodia density (β = 0.210, $p = 0.003$) and reduced thin spine head diameter (β = −0.038, $p = 0.0003$). APOE ε4 trended with increased mushroom spine length (β = 0.229, $p = 0.071$) (Table 4). Notably, in a PMI-adjusted model, the APOE ε4 allele maintained a significant association with increased filopodia density (β = 0.174, $p = 0.045$). These results highlight selective spine density and morphology changes that associate with the APOE ε4 allele in cognitively normal aging.

3.4. Alzheimer's disease pathology correlates with changes in spine density and morphology

Approximately 30%–50% of older individuals who harbor AD pathology, including Aβ plaque and NFT pathology, do not become symptomatic in their lifetime (Driscoll and Troncoso, 2011; Sperling et al., 2011). Using CERAD scores and Braak stage measurements, we examined how Aβ plaque or NFT burden, respectively, associates with spine density and morphology. Linear regressions and multivariate linear modeling were used to assess the relationship between spine phenotypes and CERAD scores or Braak stage. First, we assessed the relationship between CERAD scores and spine phenotypes by Pearson regression and an APOE-adjusted linear model. No correlations were observed with overall spine density and CERAD scores or Braak stage (Fig. 5A–B). By simple regression, CERAD scores correlated with increased spine length (r = 0.456, $p = 0.017$) (Fig. 5G), but we detected no relationships involving mean lengths of individual spine classes (Table 5). CERAD scores correlated with reduced stubby spine density (r = −0.411, $p = 0.029$), increased filopodia density (r = 0.399, $p = 0.033$), and reduced thin spine head diameter (r = −0.519, $p = 0.007$) (Fig. 5C, E, K, Table 5). After adjusting for APOE ε4 status, CERAD scores significantly correlated with thin spine head diameter (β = −0.008, $p = 0.031$). Although not reaching significance, CERAD scores trended with spine length (β = 0.069, $p = 0.120$) and stubby spine density (β = −0.353, $p = 0.151$) in the APOE ε4–adjusted model (Table 5). In a PMI-adjusted model, the CERAD score did not maintain a significant association with increased filopodia density (β = 0.036, $p = 0.244$). By Pearson regression, Braak stage associated with increased spine length (r = 0.542, $p = 0.005$), which involved

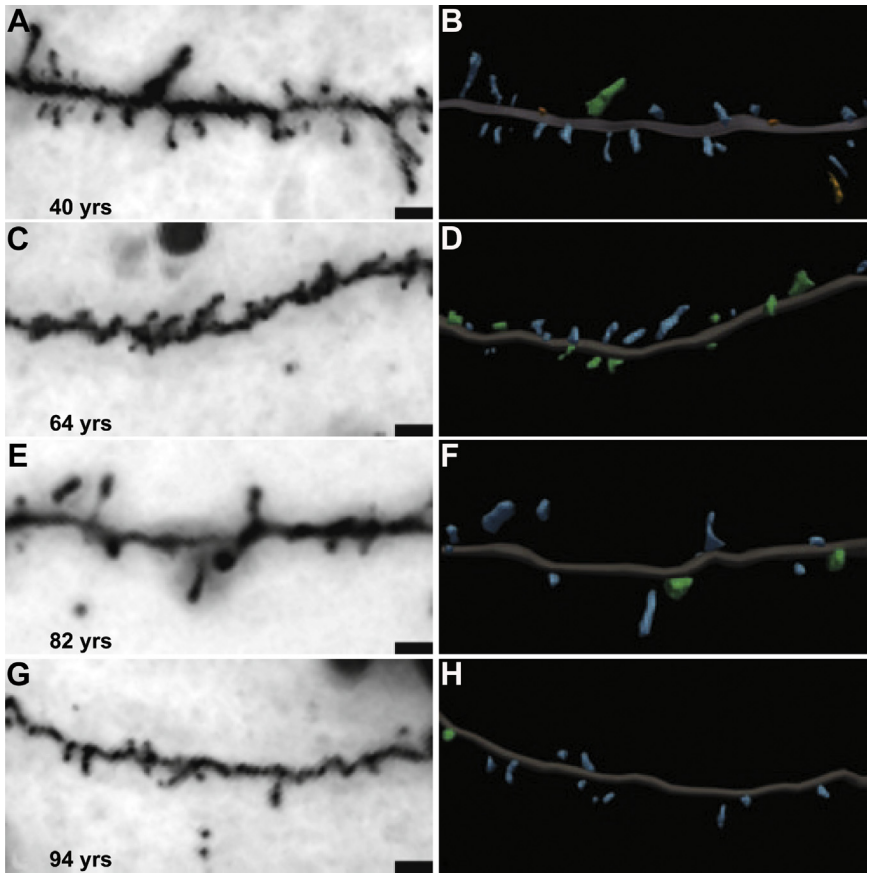

Fig. 1. Highly optimized three-dimensional modeling of dendritic spines in humans. (A, C, E, G) Representative brightfield images of Golgi-impregnated dendrites from 40-, 64-, 82-, and 94-year-old individuals. Scale bars represent 3 μm. (B, D, F, H) Three-dimensional digital reconstructions of the same dendrites generated in Neurolucida 360. Thin spines are blue, stubby spines are orange, mushroom spines are green, and filopodia are yellow. (For interpretation of the references to color in this figure legend, the reader is referred to the Web version of this article.)

increased mean length of thin ($r = 0.426$, $p = 0.024$), stubby ($r = 0.496$, $p = 0.009$), and mushroom ($r = 0.367$, $p = 0.047$) spine populations (Fig. 5H, Table 5). Moreover, Braak stage correlated with reduced stubby spine density ($r = -0.527$, $p = 0.006$), increased filopodia density ($r = 0.469$, $p = 0.014$), and reduced thin spine head diameter ($r = -0.384$, $p = 0.039$) (Fig. 5D, F, L, Table 5). Next, we examined these relationships in an APOE ε4–adjusted model with Braak stage as a predictor of each spine phenotype. After adjusting for ε4 status, Braak stage maintained a significant association with spine length ($\beta = 0.105$, $p = 0.012$), stubby spine density ($\beta = -0.581$, $p = 0.011$), filopodia density ($\beta = 0.065$, $p = 0.013$), and thin spine head diameter ($\beta = -0.008$, $p = 0.025$) (Table 5). In a PMI-adjusted model, the Braak stage trended with increased filopodia density ($\beta = 0.055$, $p = 0.064$). Together, these data indicated that Braak stage progression and increasing CERAD scores associate with similar patterns of DLPFC spine structure remodeling in elderly cognitively normal patients.

4. Discussion

In this study, we used three-dimensional modeling of dendritic spine populations in combination with linear regression analyses to identify distinct patterns of DLPFC spine remodeling that associate with cognitively normal aging in humans. Similar to studies in rodents and nonhuman primates, we demonstrated that spine density correlated negatively with human aging. Cumulative reduction in spine head diameters associated with higher MMSE scores. Individuals with at least a single APOE ε4 allele exhibited increased dendritic filopodia density combined with structural alterations in thin spines. Both Aβ plaque and NFT pathologies correlated with increased spine length, reduced thin spine head diameter, and increased filopodia density. By integrating common aspects of human brain aging, such as the development of AD pathology, our findings provide a basis for understanding how DLPFC dendritic spine structure changes during cognitively normal aging.

4.1. Prefrontal dendritic spine changes in human aging

Alterations in spine density and morphology are hypothesized to reflect changes in normal glutamatergic synaptic transmission and synaptic plasticity that occur throughout life, including aging. Although experimentally defined structure-function links have yet to be established, it is highly plausible that detrimental spine structural changes and/or loss of spines result in learning and memory impairments among aged mammals (Dumitriu et al., 2010; Hara et al., 2012; Morrison and Baxter, 2012). Elegant comparative studies in young versus aged rhesus monkeys revealed that selective loss of thin spines in DLPFC occurred in aging and strongly correlated with cognitive impairment in both acquisition and performance on delayed nonmatching-to-sample task (Dumitriu et al., 2010). Our studies in humans revealed a similar loss of spine density in the DLPFC with age (Fig. 2), although this was not correlated to impairment in cognitive function. The findings herein also support exquisite analysis of dendritic spines in the cingulate cortex of

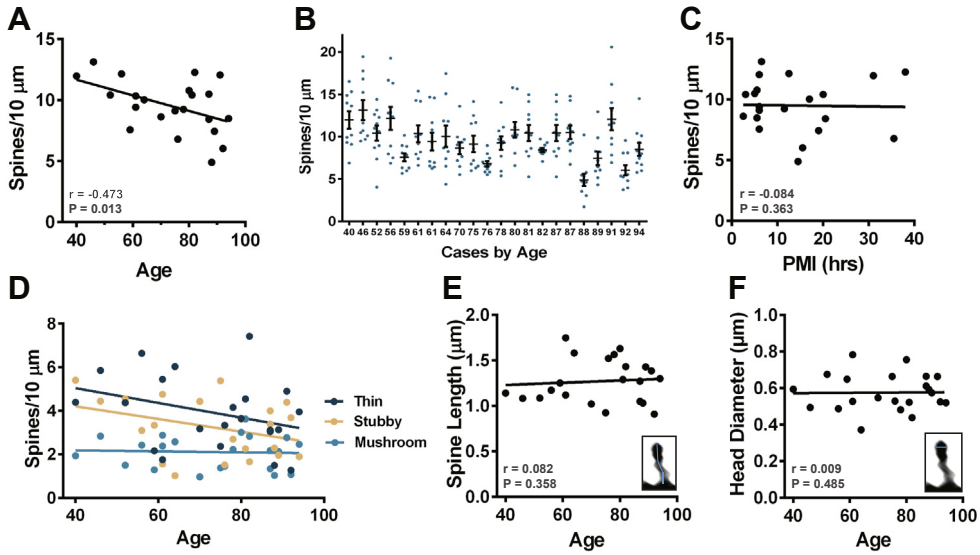

Fig. 2. Dendritic spine density is reduced in human aging. For each case, the number of spines per 10 µm was determined for 10-20 dendrites and averaged to generate a case mean. Linear regression analyses examined the relationship between age at death and individual spine phenotypes. (A) The density of spines per 10 µm of dendrite was plotted against the age of each case. Age at death is presented in years, and each dot represents one case. There is negative correlation between age and spine density. (B) Distribution of spine density measured per 10 µm of dendrite. Each dot represents the average spine density per 10 µm for each dendrite that was imaged. Individual cases represented by age in years. (C) Linear regression analysis of spine density measured per 10 µm of dendrite across all cases with PMI. Each dot represents the average spine density per 10 µm for each individual case. The density of spines per 10 µm of dendrite was plotted against the PMI for each individual. PMI represented in hours. (D) Linear regression analysis of spine classification densities measured per 10 µm of dendrite in all cases with age. Each dot represents the average spine class density per 10 µm of dendrite for each individual case. The density of spine class per 10 µm of dendrite was plotted against the age of each individual. Age represented in years. (E) Linear regression analysis examined the relationship between mean spine length and age of each case. To illustrate an example of what was measured, the inset depicts a brightfield image of a thin spine with length traced in blue. (F) Linear regression analysis examined the relationship between mean spine head diameter and age of each case. The inset depicts a brightfield image of a thin spine with head diameter traced in blue. Abbreviation: PMI, postmortem interval. (For interpretation of the references to color in this figure legend, the reader is referred to the Web version of this article.)

two humans (aged 40 and 85 years) using iontophoretic injection of single pyramidal neurons with Lucifer yellow (Benavides-Piccione et al., 2013). Our study and theirs indicate spine density loss in prefrontal regions in aging.

4.2. Genetic and pathologic aspects of Alzheimer's disease and dendritic spine remodeling

The accumulation of AD pathology in cognitively normal individuals is proposed to represent either resiliency to dementia or preclinical stages of AD (Driscoll and Troncoso, 2011; Sperling et al., 2011). These individuals provide a model to explore mechanisms that are (1) critical for retaining cognitive function in the face of AD pathology (i.e., cognitive resilience) or (2) related to the transition from preclinical to symptomatic AD. Numerous reports demonstrate that synaptic markers and/or dendritic spine loss correlates more strongly with cognitive impairment in AD than Aβ plaques or NFTs (Boros et al., 2017; DeKosky and Scheff, 1990; Terry et al., 1991). Therefore, the ability to maintain cognitive function in an environment of AD pathology must be linked to the preservation and maintenance of synapses in cognitively normal aging. We hypothesize that these individuals represent patients at risk for developing AD, and around the time of dementia onset, each individual will display varying levels of positive or negative resilience. The observations presented in this report support our hypothesis that structural remodeling of dendritic spines promotes cognitive function in the presence of AD pathology or genetic susceptibility to AD. For instance, cumulative increases in spine length through the DLPFC and increased filopodia density could maintain degenerating connections in a toxic environment or promote synaptogenesis with available axonal partners. Thin spines and filopodia are highly dynamic, plastic structures that are remodeled rapidly in response

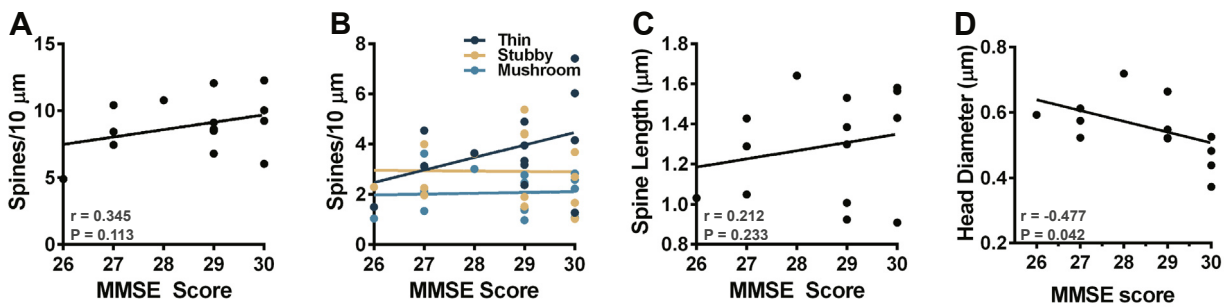

Fig. 3. Mini–Mental State Examination (MMSE) score associates with dendritic spine head diameter. (A) The relationship between the spine density per 10 µm and MMSE score was plotted. (B) Linear regression analysis of spine classification densities measured per 10 µm of dendrite in all cases with the MMSE score. Each dot represents the average spine class density per 10 µm for each individual case. (C) The relationship between the spine length and MMSE score was plotted for each case. (D) The relationship between the spine head diameter and MMSE score was plotted for each case.

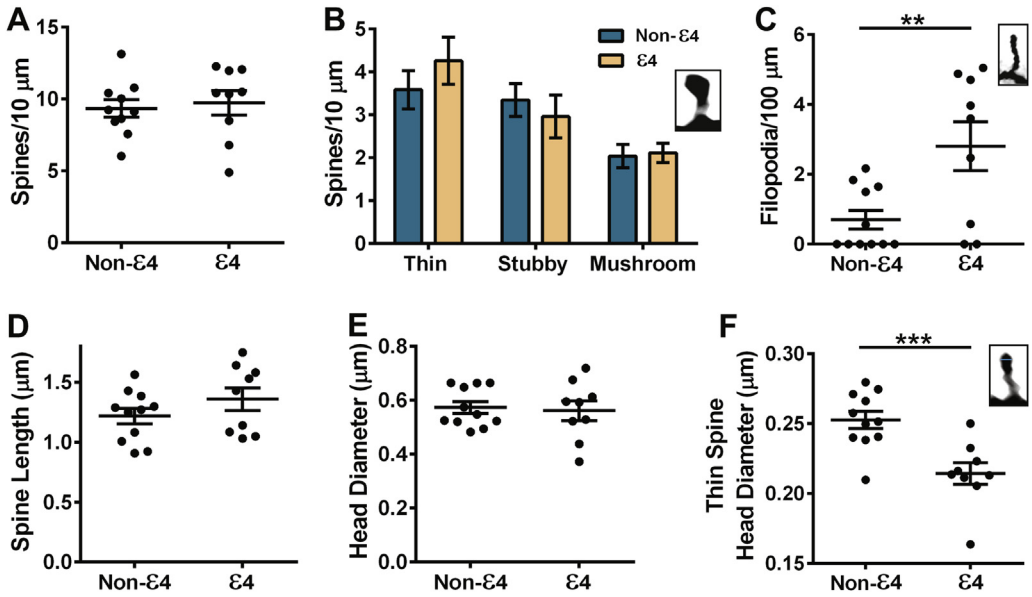

Fig. 4. Increased filopodia density and reduced thin spine head diameter associate with the APOE ε4 allele. (A) Mean number of spines per 10 µm was calculated for each case and plotted based on ε4 status. (B) Mean number of spine classification densities per 10 µm was calculated for each case and plotted based on ε4 status. The inset depicts a brightfield image of a mushroom spine. (C) Mean number of filopodia per 100 µm was calculated for each case and plotted based on ε4 status. The inset depicts a brightfield image of a filopodia. (D) Mean spine length was determined for each case and plotted based on ε4 status. (E) Mean spine head diameter was determined for each case and plotted based on ε4 status. (F) Mean head diameter of thin spines was determined for each case and plotted based on ε4 status. To illustrate an example of what was measured, the inset depicts the brightfield image of a thin spine with head diameter traced in blue. Lines represent the mean ± standard error of the mean. $^{**}p = 0.008$ and $^{***}p = 0.001$. (For interpretation of the references to color in this figure legend, the reader is referred to the Web version of this article.)

to neurotransmission and information storage (Grutzendler et al., 2002; Holtmaat et al., 2005). The changes in thin spine head diameter and length could reflect structural remodeling of thin spines, and this mechanism may provide a basis for rapid plasticity to support the complex integration and higher-order processing of the DLPFC under the burden of progressive AD pathology (Bloss et al., 2011; Boros et al., 2017; Dumitriu et al., 2010). This interpretation can be considered alongside neuroimaging research that explored the epidemiological phenomena of cognitive reserve and neural compensation in older individuals with brain pathology (Oh et al., 2018; Stern, 2012). Individuals with greater cognitive reserve may exhibit the ability to recruit alternate circuits or to attain greater activation during challenging tasks.

Given the risk for AD onset that is conferred by the APOE ε4 allele, we compared spine density and morphology between ε4 and non-ε4 carriers in cognitively normal aging. Increased filopodia density and reduced thin spine head diameter were observed among APOE ε4 allele carriers. These findings are similar to correlations between CERAD scores or Braak stage and spine phenotypes. It is extremely challenging to uncouple the putative neurobiological influence of the APOE ε4 allele versus AD pathology on spine characteristics under these experimental conditions. However, our findings do suggest that cognitively normal APOE ε4 carriers do exhibit a relatively selective spine morphologic profile in the DLPFC, featuring concomitant structural alterations in thin and mushroom spines. These phenotypes in addition to populous filopodia strengthen the growing idea that dendritic structural plasticity may provide a basis for positive resilience against dementia onset.

4.3. Strengths and limitations of imaging Golgi-Cox stain in human samples

A major strength of Golgi-Cox stain is the ability to study neuron structure in postmortem human brain tissue samples on a broad scale. Various immersion fixation protocols, including but not limited to paraformaldehyde and formalin, are amenable to Golgi-Cox stain, making this impregnation strategy the only method suitable for collective studies of human tissue from brain banks around the world. The limitation of Golgi-Cox stain for dendritic microstructure analyses is that images must be collected using transmitted light brightfield microscopy. Digital images collected in this manner contain out-of-focus light haze and blur, requiring the experimenter to tediously trace through the image in x, y, and z dimensions to reconstruct dendrites in morphometry software. Future studies could use blind deconvolution as a possible solution to the caveats of out-of-focus light that are captured using brightfield microscopy (Holmes and O'Connor, 2000). Nyquist sampling of fluorescently labeled neurons using a laser scanning confocal microscope followed by post hoc deconvolution is arguably a better methodology to study dendritic microstructure (Dumitriu et al., 2011). This imaging strategy provides the highest resolution in diffraction-limited microscopy; however, human brain tissue samples must be prepared under highly optimal conditions at autopsy (Benavides-Piccione et al., 2013). These sample preparation requirements deem fluorescence-based confocal imaging methods impossible for large-scale dendritic morphology studies of humans.

4.4. Future clinical implications of structural plasticity

The advent of novel radioactive tracers for positron emission tomography (PET) that can target Aβ or tau pathology permits the visualization of AD progression in vivo (Rowe et al., 2013; Scholl et al., 2016). These exciting strategies confirm and reinforce the decades of postmortem studies that painstakingly mapped AD pathology using cross-sectional intervals. Using the findings here, a comparison of PET tau imaging and its correlative Braak stage could be used to extrapolate a hypothetical representation of spine structure in the DLPFC of cognitively normal patients. Our methods provide robust acquisition of spine data across brain regions and ties cellular changes to cognitive function in aging. With additional

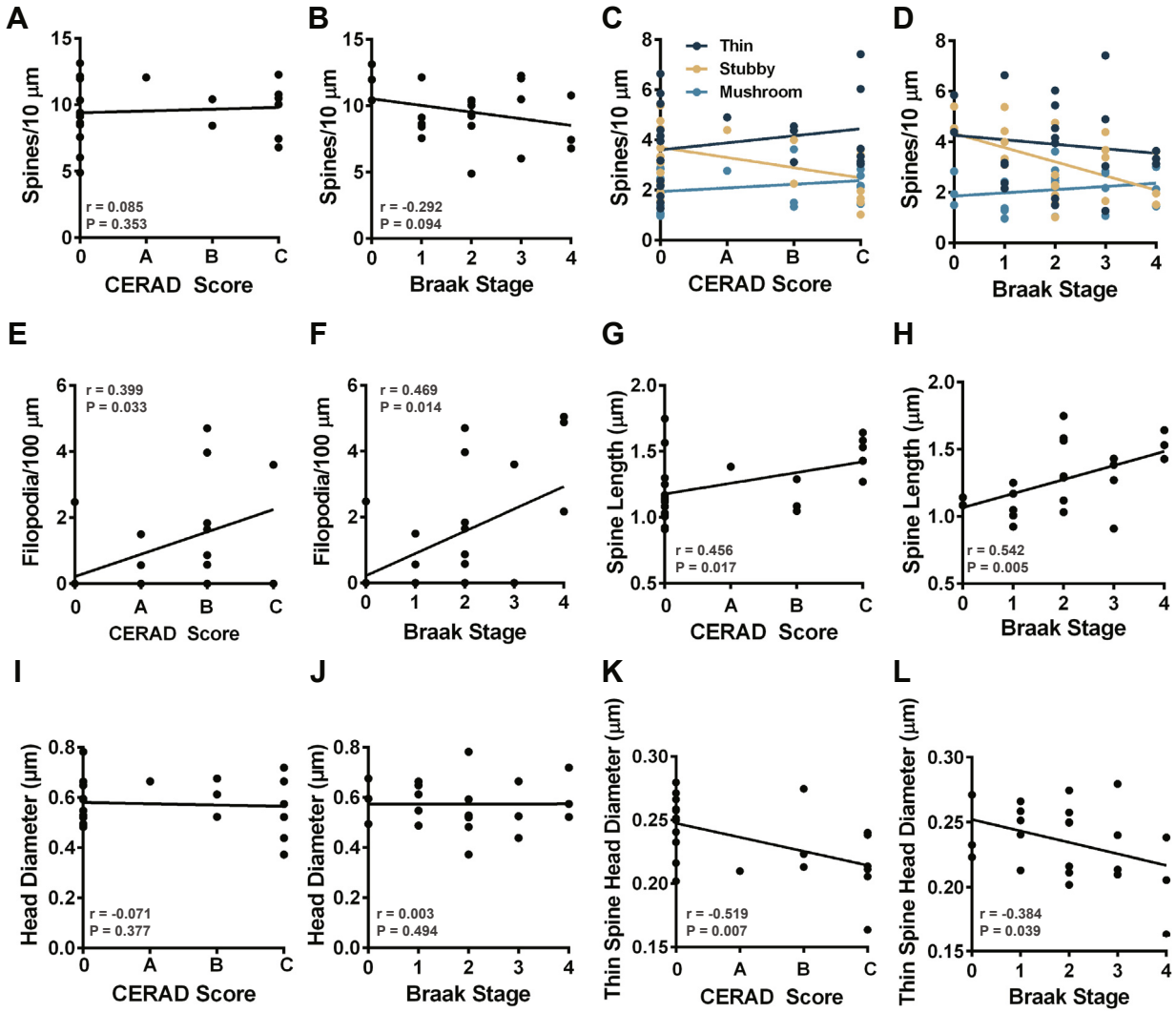

Fig. 5. Selective spine phenotypes associate with CERAD score or Braak stage. (A) The relationship between the spine density per 10 µm and CERAD score was plotted. (B) The relationship between the spine density per 10 µm and Braak stage was plotted. (C) Linear regression analysis of spine classification densities measured per 10 µm of dendrite in all cases with the CERAD score. Each dot represents the average spine class density per 10 µm for each individual case. (D) Linear regression analysis of spine classification densities measured per 10 µm of dendrite in all cases with Braak stage. Filopodia density per 100 µm was plotted against (E) CERAD score or (F) Braak stage for each case. The relationship between spine length and (G) CERAD score or (H) Braak stage was plotted for each case. The relationship between spine head diameter and (I) CERAD score or (J) Braak stage was plotted for each case. Linear regression analysis detected a negative relationship between (K) CERAD score or (L) Braak stage and thin spine head diameter.

future studies, these measures will provide an unprecedented map of spine morphology at various stages of human aging. Currently, this analysis can only be conducted on postmortem samples; however, recent advances in PET suggest the possibility of synaptic density measurements in living humans (Finnema et al., 2016). Our findings begin to lay the foundation for cellular biomarkers of spine loss or remodeling once PET reaches higher resolutions.

Disclosure statement

The authors have nothing to disclose and have no conflicts of interest.

Acknowledgements

This work was supported by the National Institutes of Health through NIA AG061800, NIA AG054719, and NIA AG043552 to JHH; Emory Neuroscience NINDS Core Facilities grant P30NS055077; and the Emory University Alzheimer's Disease Research Center grant AG025688. Additional support stemmed from a New Investigator Research Grant 2015-NIRG-339422 to JHH from the Alzheimer's Association.

References

Alvarez, V.A., Sabatini, B.L., 2007. Anatomical and physiological plasticity of dendritic spines. Annu. Rev. Neurosci. 30, 79–97.

Bai, L., Hof, P.R., Standaert, D.G., Xing, Y., Nelson, S.E., Young, A.B., Magnusson, K.R., 2004. Changes in the expression of the NR2B subunit during aging in macaque monkeys. Neurobiol. Aging 25, 201–208.

Barnes, C.A., Suster, M.S., Shen, J., McNaughton, B.L., 1997. Multistability of cognitive maps in the hippocampus of old rats. Nature 388, 272–275.

Benavides-Piccione, R., Ballesteros-Yanez, I., DeFelipe, J., Yuste, R., 2002. Cortical area and species differences in dendritic spine morphology. J. Neurocytol. 31, 337–346.

Benavides-Piccione, R., Fernaud-Espinosa, I., Robles, V., Yuste, R., DeFelipe, J., 2013. Age-based comparison of human dendritic spine structure using complete three-dimensional reconstructions. Cereb. Cortex. 23, 1798–1810.

Bloss, E.B., Janssen, W.G., Ohm, D.T., Yuk, F.J., Wadsworth, S., Saardi, K.M., McEwen, B.S., Morrison, J.H., 2011. Evidence for reduced experience-dependent

dendritic spine plasticity in the aging prefrontal cortex. J. Neurosci. 31, 7831–7839.
Boros, B.D., Greathouse, K.M., Gentry, E.G., Curtis, K.A., Birchall, E.L., Gearing, M., Herskowitz, J.H., 2017. Dendritic spines provide cognitive resilience against Alzheimer's disease. Ann. Neurol. 82, 602–614.
Burke, S.N., Barnes, C.A., 2006. Neural plasticity in the ageing brain. Nat. Rev. Neurosci. 7, 30–40.
Chang, F.L., Greenough, W.T., 1984. Transient and enduring morphological correlates of synaptic activity and efficacy change in the rat hippocampal slice. Brain Res. 309, 35–46.
Corder, E.H., Saunders, A.M., Strittmatter, W.J., Schmechel, D.E., Gaskell, P.C., Small, G.W., Roses, A.D., Haines, J.L., Pericak-Vance, M.A., 1993. Gene dose of apolipoprotein E type 4 allele and the risk of Alzheimer's disease in late onset families. Science 261, 921–923.
Cupp, C.J., Uemura, E., 1980. Age-related changes in prefrontal cortex of Macaca mulatta: quantitative analysis of dendritic branching patterns. Exp. Neurol. 69, 143–163.
DeKosky, S.T., Scheff, S.W., 1990. Synapse loss in frontal cortex biopsies in Alzheimer's disease: correlation with cognitive severity. Ann. Neurol. 27, 457–464.
Dickstein, D.L., Weaver, C.M., Luebke, J.I., Hof, P.R., 2012. Dendritic spine changes associated with normal aging. Neuroscience 251, 21–32.
Driscoll, I., Troncoso, J., 2011. Asymptomatic Alzheimer's disease: a prodrome or a state of resilience? Curr. Alzheimer Res. 8, 330–335.
Duan, H., Wearne, S.L., Rocher, A.B., Macedo, A., Morrison, J.H., Hof, P.R., 2003. Age-related dendritic and spine changes in corticocortically projecting neurons in macaque monkeys. Cereb. Cortex. 13, 950–961.
Dumitriu, D., Hao, J., Hara, Y., Kaufmann, J., Janssen, W.G., Lou, W., Rapp, P.R., Morrison, J.H., 2010. Selective changes in thin spine density and morphology in monkey prefrontal cortex correlate with aging-related cognitive impairment. J. Neurosci. 30, 7507–7515.
Dumitriu, D., Rodriguez, A., Morrison, J.H., 2011. High-throughput, detailed, cell-specific neuroanatomy of dendritic spines using microinjection and confocal microscopy. Nat. Protoc. 6, 1391–1411.
Farrer, L.A., Cupples, L.A., Haines, J.L., Hyman, B., Kukull, W.A., Mayeux, R., Myers, R.H., Pericak-Vance, M.A., Risch, N., van Duijn, C.M., 1997. Effects of age, sex, and ethnicity on the association between apolipoprotein E genotype and Alzheimer disease. A meta-analysis. APOE and Alzheimer Disease Meta Analysis Consortium. JAMA 278, 1349–1356.
Finnema, S.J., Nabulsi, N.B., Eid, T., Detyniecki, K., Lin, S.F., Chen, M.K., Dhaher, R., Matuskey, D., Baum, E., Holden, D., Spencer, D.D., Mercier, J., Hannestad, J., Huang, Y., Carson, R.E., 2016. Imaging synaptic density in the living human brain. Sci. Transl. Med. 8, 348ra396.
Grutzendler, J., Kasthuri, N., Gan, W.B., 2002. Long-term dendritic spine stability in the adult cortex. Nature 420, 812–816.
Hara, Y., Rapp, P.R., Morrison, J.H., 2012. Neuronal and morphological bases of cognitive decline in aged rhesus monkeys. Age (Dordr) 34, 1051–1073.
Harris, K.M., Jensen, F.E., Tsao, B., 1992. Three-dimensional structure of dendritic spines and synapses in rat hippocampus (CA1) at postnatal day 15 and adult ages: implications for the maturation of synaptic physiology and long-term potentiation. J. Neurosci. 12, 2685–2705.
Hayashi, Y., Majewska, A.K., 2005. Dendritic spine geometry: functional implication and regulation. Neuron 46, 529–532.
Hering, H., Sheng, M., 2001. Dendritic spines: structure, dynamics and regulation. Nat. Rev. Neurosci. 2, 880–888.
Holmes, T.J., O'Connor, N.J., 2000. Blind deconvolution of 3D transmitted light brightfield micrographs. J. Microsc. 200 (Pt 2), 114–127.
Holtmaat, A., Svoboda, K., 2009. Experience-dependent structural synaptic plasticity in the mammalian brain. Nat. Rev. Neurosci. 10, 647–658.
Holtmaat, A.J., Trachtenberg, J.T., Wilbrecht, L., Shepherd, G.M., Zhang, X., Knott, G.W., Svoboda, K., 2005. Transient and persistent dendritic spines in the neocortex in vivo. Neuron 45, 279–291.
Hughes, C.P., Berg, L., Danziger, W.L., Coben, L.A., Martin, R.L., 1982. A new clinical scale for the staging of dementia. Br. J. Psychiatry 140, 566–572.
Jacobs, B., Driscoll, L., Schall, M., 1997. Life-span dendritic and spine changes in areas 10 and 18 of human cortex: a quantitative Golgi study. J. Comp. Neurol. 386, 661–680.
Jacobs, B., Schall, M., Prather, M., Kapler, E., Driscoll, L., Baca, S., Jacobs, J., Ford, K., Wainwright, M., Treml, M., 2001. Regional dendritic and spine variation in human cerebral cortex: a quantitative golgi study. Cereb. Cortex. 11, 558–571.
Kasai, H., Fukuda, M., Watanabe, S., Hayashi-Takagi, A., Noguchi, J., 2010. Structural dynamics of dendritic spines in memory and cognition. Trends. Neurosci. 33, 121–129.
Luebke, J.I., Chang, Y.M., Moore, T.L., Rosene, D.L., 2004. Normal aging results in decreased synaptic excitation and increased synaptic inhibition of layer 2/3 pyramidal cells in the monkey prefrontal cortex. Neuroscience 125, 277–288.
Majewska, A., Brown, E., Ross, J., Yuste, R., 2000a. Mechanisms of calcium decay kinetics in hippocampal spines: role of spine calcium pumps and calcium diffusion through the spine neck in biochemical compartmentalization. J. Neurosci. 20, 1722–1734.
Majewska, A., Tashiro, A., Yuste, R., 2000b. Regulation of spine calcium dynamics by rapid spine motility. J. Neurosci. 20, 8262–8268.
Michaelson, D.M., 2014. APOE epsilon4: the most prevalent yet understudied risk factor for Alzheimer's disease. Alzheimers Dement. 10, 861–868.
Mirra, S.S., Heyman, A., McKeel, D., Sumi, S.M., Crain, B.J., Brownlee, L.M., Vogel, F.S., Hughes, J.P., van Belle, G., Berg, L., 1991. The consortium to establish a registry for Alzheimer's disease (CERAD). Part II. Standardization of the neuropathologic assessment of Alzheimer's disease. Neurology 41, 479–486.
Montine, T.J., Phelps, C.H., Beach, T.G., Bigio, E.H., Cairns, N.J., Dickson, D.W., Duyckaerts, C., Frosch, M.P., Masliah, E., Mirra, S.S., Nelson, P.T., Schneider, J.A., Thal, D.R., Trojanowski, J.Q., Vinters, H.V., Hyman, B.T., 2012. National Institute on aging-Alzheimer's association guidelines for the neuropathologic assessment of Alzheimer's disease: a practical approach. Acta Neuropathol. 123, 1–11.
Morris, J.C., 1993. The Clinical Dementia Rating (CDR): current version and scoring rules. Neurology 43, 2412–2414.
Morrison, J.H., Baxter, M.G., 2012. The ageing cortical synapse: hallmarks and implications for cognitive decline. Nat. Rev. Neurosci. 13, 240–250.
Nusser, Z., Lujan, R., Laube, G., Roberts, J.D., Molnar, E., Somogyi, P., 1998. Cell type and pathway dependence of synaptic AMPA receptor number and variability in the hippocampus. Neuron 21, 545–559.
Oh, H., Razlighi, Q.R., Stern, Y., 2018. Multiple pathways of reserve simultaneously present in cognitively normal older adults. Neurology 90, e197–e205.
Page, T.L., Einstein, M., Duan, H., He, Y., Flores, T., Rolshud, D., Erwin, J.M., Wearne, S.L., Morrison, J.H., Hof, P.R., 2002. Morphological alterations in neurons forming corticocortical projections in the neocortex of aged Patas monkeys. Neurosci. Lett. 317, 37–41.
Park, J.S., Bateman, M.C., Goldberg, M.P., 1996. Rapid alterations in dendrite morphology during sublethal hypoxia or glutamate receptor activation. Neurobiol. Dis. 3, 215–227.
Parnass, Z., Tashiro, A., Yuste, R., 2000. Analysis of spine morphological plasticity in developing hippocampal pyramidal neurons. Hippocampus 10, 561–568.
Peters, A., Kaiserman-Abramof, I.R., 1970. The small pyramidal neuron of the rat cerebral cortex. The perikaryon, dendrites and spines. Am. J. Anat. 127, 321–355.
Peters, A., Rosene, D.L., Moss, M.B., Kemper, T.L., Abraham, C.R., Tigges, J., Albert, M.S., 1996. Neurobiological bases of age-related cognitive decline in the rhesus monkey. J. Neuropathol. Exp. Neurol. 55, 861–874.
Peters, A., Sethares, C., Luebke, J.I., 2008. Synapses are lost during aging in the primate prefrontal cortex. Neuroscience 152, 970–981.
Peters, A., Sethares, C., Moss, M.B., 1998. The effects of aging on layer 1 in area 46 of prefrontal cortex in the rhesus monkey. Cereb. Cortex. 8, 671–684.
Petralia, R.S., Mattson, M.P., Yao, P.J., 2014. Communication breakdown: the impact of ageing on synapse structure. Ageing Res. Rev. 14, 31–42.
Rask-Andersen, H., Tylstedt, S., Kinnefors, A., Illing, R., 2000. Synapses on human spiral ganglion cells: a transmission electron microscopy and immunohistochemical study. Hear. Res. 141, 1–11.
Rowe, C.C., Bourgeat, P., Ellis, K.A., Brown, B., Lim, Y.Y., Mulligan, R., Jones, G., Maruff, P., Woodward, M., Price, R., Robins, P., Tochon-Danguy, H., O'Keefe, G., Pike, K.E., Yates, P., Szoeke, C., Salvado, O., Macaulay, S.L., O'Meara, T., Head, R., Cobiac, L., Savage, G., Martins, R., Masters, C.L., Ames, D., Villemagne, V.L., 2013. Predicting Alzheimer disease with beta-amyloid imaging: results from the Australian imaging, biomarkers, and lifestyle study of ageing. Ann. Neurol. 74, 905–913.
Saunders, A.M., Strittmatter, W.J., Schmechel, D., George-Hyslop, P.H., Pericak-Vance, M.A., Joo, S.H., Rosi, B.L., Gusella, J.F., Crapper-MacLachlan, D.R., Alberts, M.J., 1993. Association of apolipoprotein E allele epsilon 4 with late-onset familial and sporadic Alzheimer's disease. Neurology 43, 1467–1472.
Scholl, M., Lockhart, S.N., Schonhaut, D.R., O'Neil, J.P., Janabi, M., Ossenkoppele, R., Baker, S.L., Vogel, J.W., Faria, J., Schwimmer, H.D., Rabinovici, G.D., Jagust, W.J., 2016. PET imaging of tau deposition in the aging human brain. Neuron 89, 971–982.
Smith, T.D., Adams, M.M., Gallagher, M., Morrison, J.H., Rapp, P.R., 2000. Circuit-specific alterations in hippocampal synaptophysin immunoreactivity predict spatial learning impairment in aged rats. J. Neurosci. 20, 6587–6593.
Sperling, R.A., Aisen, P.S., Beckett, L.A., Bennett, D.A., Craft, S., Fagan, A.M., Iwatsubo, T., Jack Jr., C.R., Kaye, J., Montine, T.J., Park, D.C., Reiman, E.M., Rowe, C.C., Siemers, E., Stern, Y., Yaffe, K., Carrillo, M.C., Thies, B., Morrison-Bogorad, M., Wagster, M.V., Phelps, C.H., 2011. Toward defining the preclinical stages of Alzheimer's disease: recommendations from the National Institute on Aging-Alzheimer's Association workgroups on diagnostic guidelines for Alzheimer's disease. Alzheimers Dement. 7, 280–292.
Stern, Y., 2012. Cognitive reserve in ageing and Alzheimer's disease. Lancet Neurol. 11, 1006–1012.
Swanger, S.A., Mattheyses, A.L., Gentry, E.G., Herskowitz, J.H., 2015. ROCK1 and ROCK2 inhibition alters dendritic spine morphology in hippocampal neurons. Cell Logist. 5, e1133266.
Swanger, S.A., Yao, X., Gross, C., Bassell, G.J., 2011. Automated 4D analysis of dendritic spine morphology: applications to stimulus-induced spine remodeling and pharmacological rescue in a disease model. Mol. Brain 4, 38.
Tang, G., Gudsnuk, K., Kuo, S.H., Cotrina, M.L., Rosoklija, G., Sosunov, A., Sonders, M.S., Kanter, E., Castagna, C., Yamamoto, A., Yue, Z., Arancio, O., Peterson, B.S., Champagne, F., Dwork, A.J., Goldman, J., Sulzer, D., 2014. Loss of mTOR-dependent macroautophagy causes autistic-like synaptic pruning deficits. Neuron 83, 1131–1143.
Terry, R.D., Masliah, E., Salmon, D.P., Butters, N., DeTeresa, R., Hill, R., Hansen, L.A., Katzman, R., 1991. Physical basis of cognitive alterations in Alzheimer's disease:

synapse loss is the major correlate of cognitive impairment. Ann. Neurol. 30, 572–580.
Tonnesen, J., Katona, G., Rozsa, B., Nagerl, U.V., 2014. Spine neck plasticity regulates compartmentalization of synapses. Nat. Neurosci. 17, 678–685.
van Veluw, S.J., Sawyer, E.K., Clover, L., Cousijn, H., De Jager, C., Esiri, M.M., Chance, S.A., 2012. Prefrontal cortex cytoarchitecture in normal aging and Alzheimer's disease: a relationship with IQ. Brain Struct. Funct. 217, 797–808.
Wong, S., Flanagan, E., Savage, G., Hodges, J.R., Hornberger, M., 2014. Contrasting prefrontal cortex contributions to episodic memory dysfunction in behavioural variant frontotemporal dementia and Alzheimer's disease. PLoS One 9, e87778.
Young, M.E., Ohm, D.T., Dumitriu, D., Rapp, P.R., Morrison, J.H., 2014. Differential effects of aging on dendritic spines in visual cortex and prefrontal cortex of the rhesus monkey. Neuroscience 274, 33–43.
Yuste, R., Majewska, A., Holthoff, K., 2000. From form to function: calcium compartmentalization in dendritic spines. Nat. Neurosci. 3, 653–659.
Ziv, N.E., Smith, S.J., 1996. Evidence for a role of dendritic filopodia in synaptogenesis and spine formation. Neuron 17, 91–102.